ARMY RESEARCH LABORATORY

Microbolometer Detectors for Passive Millimeter-Wave Imaging

by Joseph Nemarich

ARL-TR-3460 March 2005

NOTICES

Disclaimers

The findings in this report are not to be construed as an official Department of the Army position unless so designated by other authorized documents.

Citation of manufacturer's or trade names does not constitute an official endorsement or approval of the use thereof.

Destroy this report when it is no longer needed. Do not return it to the originator.

Army Research Laboratory

Adelphi, MD 20783-1197

ARL-TR-3460 **March 2005**

Microbolometer Detectors for Passive Millimeter-Wave Imaging

Joseph Nemarich
Sensors and Electron Devices Directorate, ARL

REPORT DOCUMENTATION PAGE

Form Approved
OMB No. 0704-0188

1. REPORT DATE *(DD-MM-YYYY)*	2. REPORT TYPE	3. DATES COVERED (From - To)
March 2005	Final	FY04 to FY05

4. TITLE AND SUBTITLE
Microbolometer Detectors for Passive Millimeter-Wave Imaging

5a. CONTRACT NUMBER

5b. GRANT NUMBER

5c. PROGRAM ELEMENT NUMBER

6. AUTHOR(S)
Joseph Nemarich

5d. PROJECT NUMBER

5e. TASK NUMBER

5f. WORK UNIT NUMBER

7. PERFORMING ORGANIZATION NAME(S) AND ADDRESS(ES)
U.S. Army Research Laboratory
ATTN: AMSRD-ARL-SE-RM
2800 Powder Mill Road
Adelphi, MD 20783-1197

8. PERFORMING ORGANIZATION REPORT NUMBER
ARL-TR-3460

9. SPONSORING/MONITORING AGENCY NAME(S) AND ADDRESS(ES)
U.S. Army Research Laboratory
2800 Powder Mill Road
Adelphi, MD 20783-1197

10. SPONSOR/MONITOR'S ACRONYM(S)

11. SPONSOR/MONITOR'S REPORT NUMBER(S)

12. DISTRIBUTION/AVAILABILITY STATEMENT
Approved for public release; distribution unlimited.

13. SUPPLEMENTARY NOTES

14. ABSTRACT

Reports on far-infrared and infrared microbolometer detectors developed with cooled high temperature superconductor (HTSC) materials were reviewed to determine whether it would be feasible to use this type of detector in a passive millimeter wave camera (PMC). A base-line set of achievable HTSC microbolometer parameter values were identified and used to calculate the noise equivalent temperature difference (NETD) of a cooled MMW radiometer with this type of detector. The report includes results showing that the calculated NETD of such a radiometer operating at a 30-Hz modulation frequency would be between 3 and 6 K for an RF bandwidth between 70 and 40 GHz. A PMC with this NETD would be competitive with that of previously developed systems, be much less costly, and be suitable for a number of applications. The results of further calculations made to determine the HTSC microbolometer parameter values needed to obtain an improved MMW detector are included in the report.

15. SUBJECT TERMS
Millimeter waves, passive MMW imaging, MMW detectors, microbolometers

16. SECURITY CLASSIFICATION OF:			17. LIMITATION OF ABSTRACT	18. NUMBER OF PAGES	19a. NAME OF RESPONSIBLE PERSON
a. REPORT	b. ABSTRACT	c. THIS PAGE			Joseph Nemarich
Unclassified	Unclassified	Unclassified	UL	43	19b. TELEPHONE NUMBER (*Include area code*) 301-394-3172

Standard Form 298 (Rev. 8/98)
Prescribed by ANSI Std. Z39.18

Contents

List of Figures iv

List of Tables iv

Acknowledgements vii

1. Introduction 1

2. MMW Microbolometers for Thermal Imaging 2

2.1 Architecture of a MMW Microbolometer Detector 2

2.2 Figures of Merit....5

2.2.1 Noise Equivalent Power 5

2.2.2 Noise Equivalent Temperature Difference....10

3. Status of Microbolometer Developments 11

3.1 Uncooled MMW/Sub-MMW Detectors....11

3.2 Uncooled Infrared Detectors 13

3.3 Cooled Far-Infrared/Infared Detectors....14

4. MMW Cooled Microbolometer Detector 16

4.1 NEP* of a HTSC Microbolometer Element....16

4.2 NETD of a MMW Radiometer with an HTSC Microbolometer Detector....24

5. Discussion 26

6. Conclusions 28

7. References 29

Distribution List 33

List of Figures

Figure 1. Architecture of a radiometer with microbolometer detection. 3
Figure 2. Architecture of a microbolometer. 3
Figure 3. Simplified schematics of an antenna-coupled MMW microbolometer element and antenna (*9, 10*). 4
Figure 4. NETD of an uncooled MMW radiometer shown plotted as a function of the NEP of its microbolometer detector for three values of the RF bandwidth, B_{RF}. The video bandwidth, B_V, was taken to be 30 Hz, and the transmission efficiency of the primary collecting optics, ρ_0, was 0.50. The NETD's calculated for the NEP = 12 pW/(Hz)$^{1/2}$, reported by Anderson et al., (*10*), are indicated..... 13
Figure 5. Curves showing the dependence of NEP* on f_m when both G and τ are varied while C and all other parameters are kept constant. The other parameters used for the calculations are listed in table 5. 20
Figure 6. Curves showing the dependence of NEP* on f_m when both C and τ are varied while G and all other parameters are kept constant. The other parameters used for the calculations are listed in table 5. 21
Figure 7. Curves showing the dependence of NEP* on f_m when only α is varied. All other parameters used for the calculations are listed in table 5..... 22
Figure 8. Curves showing the dependence of NEP* on f_m for several values of n..... 23
Figure 9. Curves showing the dependence of NEP* on f_m when both G and C are varied, but τ is kept constant. The other parameters used for the calculations are listed in table 5. 24
Figure 10. NETD of a cooled MMW radiometer shown plotted as a function the NEP of its HTSC microbolometer detector for three values of the RF bandwidth, B_{RF}. The video bandwidth, B_V, was taken to be 30 Hz, and the transmission efficiency of the primary collecting optics, ρ_o, was 0.5. The NETD's corresponding to detector NEP's equal to 0.09 and 0.29 pW/(Hz)$^{1/2}$ are indicated..... 25

List of Tables

Table 1. Characteristics of several uncooled MMW and sub-MMW microbolometer detectors. Listed for each is its electrical noise equivalent power, NEP*, except for the one noted. Also listed for each are the bolometer film and substrate materials, the radiation frequency, ν, the modulation frequency, f_m, and the thermal time constant, τ. 11
Table 2. Characteristics of several uncooled infrared microbolometers focal- plane-array detectors. Listed for each is its NETD and the materials used for its bolometer film and substrate. λ gives the wavelength range and f_m is the modulation frequency used for the measurement. 14

Table 3. Characteristics of several far-infrared/infrared cooled HTSC microbolometer detectors. The NEP and the type of material used for the bolometer and its substrate are listed for each. λ is the wavelength range and f_m is the modulation frequency used for the measurements. The thermal time constant, τ, also is listed. 15
Table 4. Selected values of the basic parameters of HTSC microbolometer elements that have been reported in the literature. 16
Table 5. The various sets of values of the basic parameters of a HTSC microbolometer element that were used to calculate the electrical noise equivalent power, NEP*, of the element as a function of the modulation frequency, f_m. Also listed for each case is the value of the thermal time constant $\tau = C/G$. Case 1 is termed the base-line case. 17
Table 6. HTSC microbolometer element electrical voltage responsivities, S_V*'s, the noise voltages for each of the intrinsic noise sources, and the total intrinsic noise voltages, V_n's, calculated for various values of the modulation frequency, f_m. The calculations were performed using the values of the parameters given in table 5 for Case 1, the base-line case. 18
Table 7. Contributions to the HTSC microbolometer element's total NEP* by each of the intrinsic noise sources, and NEP* calculated for various values of the modulation frequency, f_m. The calculations were performed using the values of the voltage responsivities and noise voltages given in table 6. 18

INTENTIONALLY LEFT BLANK.

Acknowledgements

The author would like to thank David Wikner for many helpful technical discussions, and also thanks to Canh Ly and Greg Samples for their assistance in preparing the manuscript. This work was partially supported by the DARPA Microsystems Technology Office.

INTENTIONALLY LEFT BLANK

1. Introduction

There has been considerable interest for many years in passive millimeter-wave imaging (PMMWI) sensors due to the ability of this type device to obtain images during day or night, in limited visibility conditions (fog, clouds, smoke, and dust), and through most articles of clothing. The fact that these sensors do not emit any man-made radiation also is important for covert military operations and for imaging humans who may be opposed to being illuminated by any level of man-made radiation. A review paper by Yugiri et al., (*1*) contains an introduction to the physical basis for the operation of PMMWI sensors and illustrations of a number of imaging applications.

During the past decade PMMWI sensors have evolved from mechanically-scanned, single-receiver systems to staring, multiple-receiver passive millimeter-wave cameras (PMCs) (*2–5*). Systems have been developed that can operate at video frame rates of 17 to 30 Hz, and they have been extremely useful for demonstrating the possibilities for a number of applications. The down-side is that these PMCs have, in most cases, relatively complex architectures, require many MMW integrated-circuit low-noise amplifiers, and are quite costly.

Attempts have been made recently to develop MMW imaging sensors with simpler designs and lower cost receivers. These efforts have included investigations of designs employing detector arrays with microbolometers, but thus far the sensitivity of these detectors appears to be too low for most passive MMW imaging applications (*6–10*). In this report we examine what sensitivity these detectors must have to be suitable for applications and what the possibilities are for developing a sufficiently sensitive microbolometer detector array. The next section contains a review of the basics of microbolometer technology.

Past developments of microbolometer detectors have been primarily for infrared and far-infrared applications, and the important figures of merit that characterize these detectors are essentially the same as those for other types of infrared detectors. On the other hand, passive MMW imaging sensors have mostly been developed by scientists and engineers with experience in microwave and MMW detector technology. These investigators employ figures of merit that are normally used to characterize these type detectors and they are not always familiar with those figures of merit used for infrared detectors. With this in mind, a review of the basic figures of merit for infrared detectors are presented in section 2 for the benefit of those microwave and MMW investigators who might need this review. Also given in this section are expressions for these figures of merit in terms of the basic microbolometer parameters.

A summary of the performance levels achieved to date with MMW and sub-MMW microbolometer detectors are presented in section 3, and the shortfall in their ability to meet requirements for practical PMC applications is discussed. The results obtained with uncooled

infrared and cooled far-infrared/infrared microbolometers also are summarized in this section. From the summary of the performance levels achieved with the cooled far-infrared/infrared microbolometer, it may be possible to develop a MMW microbolometer with the necessary sensitivity using a high temperature superconducting (HTSC) material operating as a "transition-edge" microbolometer. In section 4 calculations are made to determine the dependence of the performance characteristics of a HTSC MMW microbolometer on the values of its basic parameters. The results of these calculations are discussed in section 5, and the conclusions reached in this report are summarized in section 6.

2. MMW Microbolometers for Thermal Imaging

2.1 Architecture of a MMW Microbolometer Detector

Bolometers have been used extensively in the past as thermal detectors of electromagnetic radiation, and the principles of their operation have been described in previous publications (*11, 12*). Interest in these sensors has been stimulated in recent years due to the application of photolithographic and micromachining technology for their fabrication. These technologies have allowed very small bolometers, termed microbolometers, to be built with increased sensitivity, shorter response time, and in focal-plane-array configurations for radiometric imaging applications.

The basic architecture of a MMW imaging radiometer with microbolometer detection is shown schematically in figure 1. Radiation from a scene incident on the aperture of the objective lens of the primary collecting optics is focused on the microbolometer array in the focal plane of the primary collecting optics. The radiation absorbed by each microbolometer in the array causes a change in its resistance and the change is detected in the readout circuit. The resultant signals are used to display an image of the scene being viewed. Each of the microbolometers in the array consists of secondary collecting "optics" and a microbolometer element. This is shown schematically in figure 2. The secondary collecting optics may consist of a miniature MMW antenna (a microantenna) that forms, together with the microbolometer element, what is said to be an "antenna-coupled" microbolometer. The size of the microantenna, and therefore of the entire focal plane array, may be reduced by use of an immersion lens placed in close proximity to the microantenna (*13, 14, 15*).

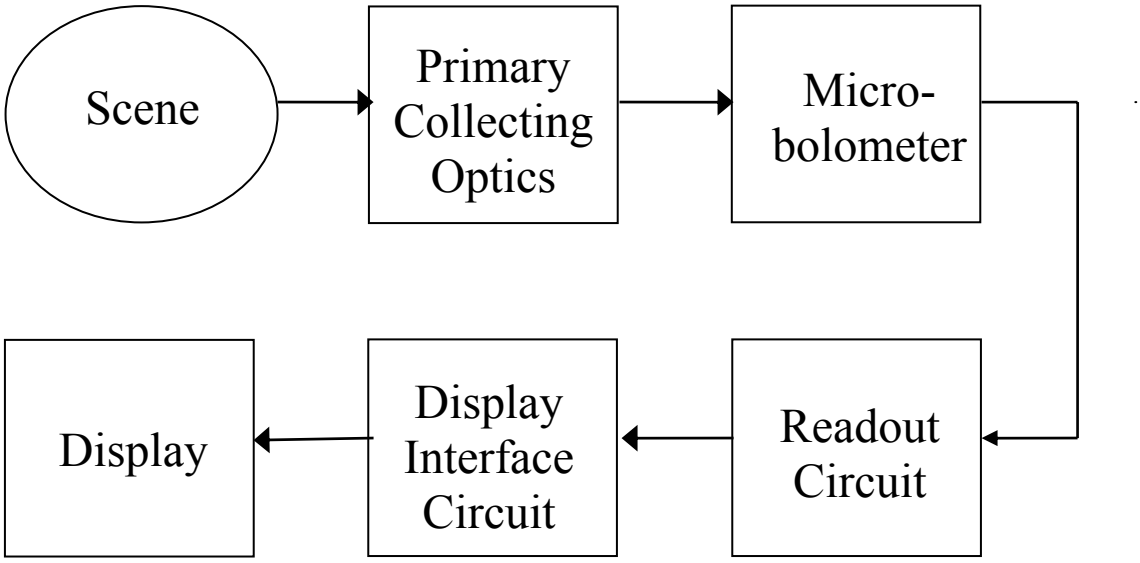

Figure 1. Architecture of a radiometer with microbolometer detection.

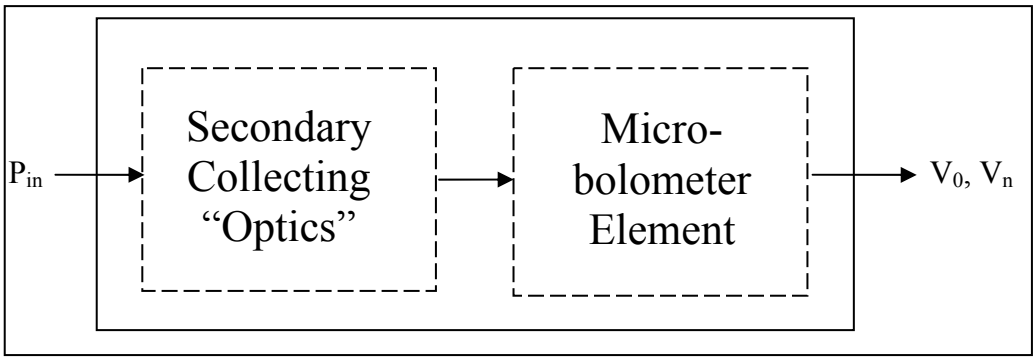

Figure 2. Architecture of a microbolometer.

Figure 3 shows simplified schematics of an antenna-coupled MMW microbolometer element and a bowtie antenna designed jointly by UCLA, HRL, and Raytheon and fabricated by a team at Raytheon (*9, 10*). In this design MMW radiation is incident on the upper surface of the bowtie antenna and also on the nichrome (NiCr) layer above the vanadium oxide (VO_x) bolometer that is partially shielding the antenna. In this microbolometer element, the antenna is capacitively coupled to the NiCr load that constitutes the lower layer of the microbolometer element. The conductive legs that are shown going from the VO_x to the Silicon (Si) substrate may be providing mechanical support for the microbolometer element (labeled "bolometer pixel") as well as electrical connections to the bolometer bias and readout circuit. These legs may be the only thermal contacts between the microbolometer element and other parts of the microbolometer structure that are in contact with the system heat sink.

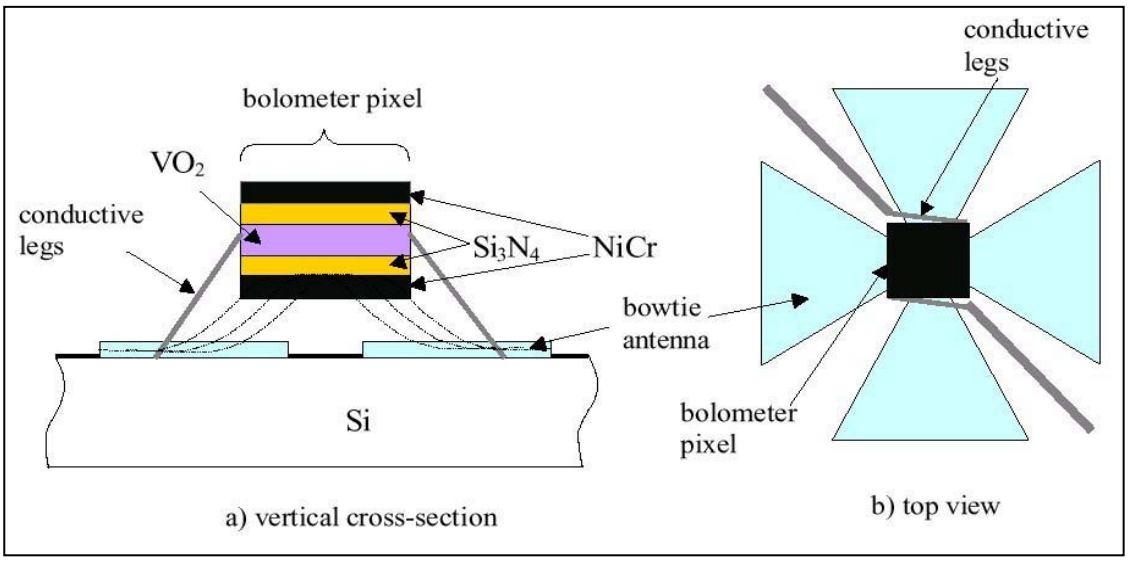

Figure 3. Simplified schematics of an antenna-coupled MMW microbolometer element and antenna (*9, 10*).

This type of microbolometer incorporates several significant design features devised by previous investigators that have led to improved microbolometer performance (*6, 7, 8, 12*). These features include the use of a composite structure, antenna-coupling, and an air-bridge. The composite structure separates the device functions for collecting the incident radiation from that for using the collected radiation to cause a detectable change in temperature. In this design, the efficiency of the radiation collector can be optimized to transfer the thermal energy to the bolometer, and the latter can be composed of a material selected to have a high temperature coefficient of resistance without the necessity for it also being an efficient collector of the incident radiation.

The importance of this antenna-coupling design feature can be understood by considering the following: the images obtained with a radiometer are enhanced by maximizing the collection of the radiation from the scene being viewed. In a radiometer with a focal-plane-array design, the radiation from the scene is focused onto diffraction-limited spots (pixels) on the focal plane of the primary collecting optics. The radiation-collection efficiency depends on how much of the radiant energy incident on each spot reaches the bolometer in the form of thermal energy.

Efficient collection may be achieved if a good radiation absorber/bolometer combination is designed to have an area that approximates the area of the diffraction-limited spot and is centered on the spot. That is, the radiation-collector should have a high "fill factor." However, the thermal time constant of the microbolometer element varies directly with its heat capacity, and a low heat capacity can be more easily achieved if the area of the microbolometer element is made smaller than that of the diffraction-limited spot. Since a microbolometer with a short thermal time constant is desirable, the antenna-coupled design helps to meet the objectives for having a radiation-collector with a high fill-factor and a microbolometer element with a shorter thermal time constant. The antenna can be designed to have an aperture area that approximates that of

the spot, and the thermal energy generated in its load may then be transferred to a much smaller bolometer element having a low heat capacity.

Another important feature of the design is the "air-bridge" that is fabricated by removing the surface layer directly below the microbolometer element using micromachining techniques. This eliminates all of the thermal conductivity contacts between the microbolometer element and the rest of the microbolometer structure, except for the legs that provide mechanical support and the electrical leads. Minimizing the thermal conductivity between the microbolometer element and the rest of the structure is essential for obtaining a highly sensitive microbolometer.

Also to be considered in the design of a MMW microbolometer is the cost of manufacturing an array which may have many hundreds of microbolometers that need to be coupled to the readout circuit. Ideally, both the microbolometer and the readout circuit should be designed to allow fabrication of a monolithic integrated device using a common established technology, such as with silicon. This should be the case with the microbolometer design described in (*9, 10*).

2.2 Figures of Merit

2.2.1 Noise Equivalent Power

Figures of merit that have been defined to characterize the performance of infrared detectors (*11–18*) are equally useful for characterizing MMW bolometers. The noise equivalent power, or NEP, is one such very commonly used figure of merit. The NEP of a detector is defined as the input power required such that the output signal-to-noise ratio equals unity. If the bolometer bias is supplied from a constant current source, the NEP of the microbolometer detector can be expressed as

$$\mathrm{NEP} = \frac{V_n}{S_V}, \tag{1}$$

where

V_n = rms noise voltage, and

S_V = voltage responsivity of the microbolometer.

S_V is defined by

$$S_V = \frac{V_o}{P_{in}}, \tag{2}$$

where

V_0 = rms output voltage, and

P_{in} = rms input RF power to the microbolometer.

V_n and V_0 are often normalized with respect to the square root of the detector video (or post-detection) bandwidth, and the NEP is then expressed in units of $W/(Hz)^{1/2}$. This convention is used in this report. In figure 2 it is seen that P_{in} is the power incident on the secondary collecting "optics" of the microbolometer, and V_o and V_n are the output and noise voltages per root Hz, respectively.

The rms noise voltage per $(Hz)^{1/2}$ can be expressed as the quadratic sum of a number of uncorrelated noise sources (*11–18*). That is,

$$V_n = [V_{1/f}^2 + V_J^2 + V_{ph}^2 + \ldots]^{1/2}, \tag{3}$$

where $V_{1/f}$ is the excess low frequency or 1/f noise voltage, V_J is the Johnson noise voltage, and V_{ph} is the phonon noise voltage. These are the main sources of intrinsic noise for the microbolometer. The preamplifier noise must be included in equation 3 if a preamplifier precedes the point where the noise and voltage outputs are measured. Other non-intrinsic noise sources that also could be listed in this equation include noise due to thermal fluctuations in the heat sink, noise due to fluctuations in thermal convection currents, noise due to vibrations, noise originating in the current or voltage bias network, and electrical pickup noise.

With care, the contribution of the non-intrinsic noise sources to the microbolometer NEP can be made negligible compared to the intrinsic noise sources, if the voltage responsivity is high. For example, the noise due to thermal fluctuations in the heat sink may be minimized if the heat sink has a large heat capacity or if the heat sink is temperature controlled, and vacuum encapsulation of the microbolometer can suppress the noise due to thermal convection currents.

Expressions have been reported for the intrinsic noise voltages and the voltage responsivity of the microbolometer element in terms of their basic parameters (*11, 12*). The results for the rms noise voltages per $(Hz)^{1/2}$ are

$$V_{1/f} = (I_B R)\,(n/f_m)^{1/2} \tag{4}$$

$$V_J = (4kTR)^{1/2}, \tag{5}$$

$$V_{ph} = (4kT^2G)^{1/2}\,S_V^*, \tag{6}$$

where

I_B = bias current

R = resistance of the microbolometer element,

n = empirical 1/f parameter (adjustable),

f_m = modulation frequency,

k = Boltzmann's constant,

T = temperature of the microbolometer element,

G = thermal conductance.

The expression for $V_{1/f}$ in equation 4 is an empirical relationship that has been found to be a good approximation for some materials for the dependence of the low frequency or 1/f noise on the modulation frequency (*19*). Other expressions also have been found to be appropriate.

S_V*, in equation 6 is the voltage responsivity of the microbolometer element that is defined by

$$S_V^* = \frac{V_o}{P_{el}}, \tag{7}$$

where P_{el} is the rms input RF power to the microbolometer element.

P_{el} is related to the input power to the microbolometer, P_{in}, by

$$P_{el} = \rho_a P_{in}, \tag{8}$$

and ρ_a is the transmission efficiency of the secondary collecting optics.

From equations 3, 4, 5, and 6, if non-intrinsic noise sources are excluded, V_n can be expressed as

$$V_n = [(I_B R)^2 (n/f_m) + 4kTR + (4kT^2G) S_V{*}^2]^{1/2} \tag{9}$$

From the above, the noise equivalent power of the microbolometer element can be expressed as

$$NEP^* = \frac{V_n}{S_v^*}. \tag{10}$$

An expression for S_V* as a function of the basic parameters of the microbolometer element has been derived from the heat balance equation 11, 12. The expression is

$$S_V^* = \frac{\alpha I_B R}{G_e \left[1 + (2\pi f_m \tau_e)^2\right]^{\frac{1}{2}}}, \tag{11}$$

where

α = temperature coefficient of resistance,

G_e = effective thermal conductance,

τ_e = effective thermal time constant, and the parameters α, G_e, and τ_e are

$$\alpha = \frac{1}{R}\frac{dR}{dT}, \tag{12}$$

$$G_e = G - \alpha I_B^2 R, \tag{13}$$

and

$$\tau_e = \frac{C}{G_e}. \tag{14}$$

where

C = heat capacity of the microbolometer element.

Note that there is a "rolloff" in the magnitude of the voltage responsivity of the microbolometer element with increasing modulation frequency due to the rolloff coefficient, $[1 + (2\pi f_m \tau_e)^{1/2}]^{1/2}$ in the denominator of equation 11.

The effective thermal conductance, G_e, is a modification of the thermal conductance, G, due to the electrothermal effect. This effect comes about because the bias power dissipated in the bolometer changes when the received radiation causes a change in the bolometer resistance. If the bolometer temperature coefficient of resistance, α, is positive and the bias is supplied by a constant current source, the received radiation will cause the bolometer resistance to increase and more bias power will be dissipated in the bolometer. The net effect of this will be to compensate somewhat for the heat loss due to the thermal conductance, G. This positive electrothermal feedback results in an effective thermal conductance, G_e, that is less than G and, therefore, an effective thermal time constant, τ_e, that is longer than τ. If the bias current is not limited, the radiation may cause a continuous increase in the bolometer bias power until G_e becomes less than zero and the bolometer is destroyed by the "thermal runaway."

An electrothermal instability coefficient, a, may be defined by

$$a = \alpha I_B^2 R/G, \tag{15}$$

Then

$$G_e = (1-a)G, \tag{16}$$

and the limiting value of the bias current can be determined by setting a maximum value for a. This value is frequently chosen to be 0.3, to insure that thermal runaway does not occur (*19*).

If the bias is supplied by a constant voltage source and α is positive, the radiation will cause the bias current to decrease and less bias power will be dissipated in the bolometer. The net effect of this negative electrothermal feedback will be that G_e will be greater than G and τ_e will be less than τ (*20*).

If α is negative, the electrothermal feedback will be positive if the bias is from a constant voltage source and negative if it is from a constant current source.

From equations 9, 10, and 11, NEP* also can be expressed in terms of the basic parameters of the microbolometer element. That is,

$$NEP^* = \left\{ \left(\frac{n}{f_m}\right)\left(\frac{G_e}{\alpha}\right)^2 \left[1 + (2\pi f_m \tau_e)^2\right] + \left(\frac{4kT}{I_B^2 R}\right)\left(\frac{G_e}{\alpha}\right)^2 \left[1 + (2\pi f_m \tau_e)^2\right] + 4kT^2 G \right\}^{\frac{1}{2}} \tag{17}$$

The right side of equation 17 can be seen to be the root of the quadratic sum of $NEP_{1/f}$*, the low frequency noise contribution to NEP*, and NEP_J*, the Johnson noise contribution, and NEP_{ph}*, the phonon noise contribution, respectively. At low modulation frequencies, if S_V* is sufficiently high, $NEP_{1/f}$* decreases as f_m increases until $NEP_{1/f}$* may equal NEP_{ph}*. The frequency at which this occurs is designated here as f_{mL}. In the literature this frequency is sometimes called the "knee frequency." If S_V* is sufficiently high at this frequency, NEP_J* also may be less than NEP_{ph}*, and NEP* is then said to be at the phonon noise limit. However, as f_m increases the S_V* rolloff coefficient increases until NEP_J* = NEP_{ph}*. The modulation frequency at which this occurs is designated here as f_{mH}, the frequency above which NEP* is no longer at the phonon noise limit. Hence, given the appropriate set of values for the parameters of the microbolometer element, there can be a window of frequencies (between f_{mL} and f_{mH}) where NEP* is at the phonon noise limit.

Equation 18 for NEP* also can be expressed in terms of the electrothermal instability coefficient, a, and the basic parameters of the microbolometer element. That is,

$$NEP^* = \left\{ \begin{array}{l} (1-a)^2 \left(\frac{n}{f_m}\right)\left(\frac{G}{\alpha}\right)^2 \left[1+\left(\frac{2\pi}{1-a}\right)^2 (f_m \tau)^2\right] \\ +\frac{(1-a)^2}{a}\left(\frac{4kTG}{\alpha}\right)\left[1+\left(\frac{2\pi}{1-a}\right)^2 (f_m \tau)^2\right] \\ +4kT^2G \end{array} \right\}^{\frac{1}{2}} \qquad (18)$$

Note that the variables I_B and R no longer appear explicitly in equation 18, but instead the product of I_B^2R is constrained by equation 15 and the values of a, α, and G. However, the value of R may be predetermined when the choice is made for the microbolometer film material and its dimensions. In that case, the maximum safe value for the bias current will be determined from equation 15 and the values of a, α, G, and R. The net effect of expressing NEP* in the form given by equation 18 is that, once the value of a has been selected, the number of parameters that determine the magnitude of NEP* will have been reduced by two.

From equations 2, 7, and 8, S_V, the voltage responsivity of the microbolometer, and S_V*, the voltage responsivity of the microbolometer element, can be seen to be related. That is

$$S_V = \rho_a S_V^*. \qquad (19)$$

Hence, it follows that NEP* and NEP are related by

$$NEP^* = \rho_a NEP \quad . \qquad (20)$$

NEP*, the noise equivalent power of the microbolometer element, derived from S_V*, is often termed the "electrical noise equivalent power," (or NEP_e), whereas NEP, the noise equivalent

power of the microbolometer, derived from S_V, is often termed the "optical noise equivalent power," (or NEP_o). From equation 20 it is seen that the electrical noise equivalent power, NEP*, is always lower than the optical noise equivalent power, NEP.

NEP* may be found from equation 10 and independent determinations of V_n and S_V*. The rms noise voltage, V_n, is obtained from electrical measurements, and the voltage responsivity of the microbolometer element, S_V*, can be found by one of two methods. In one way, S_V* may be calculated from equation 11, if the basic parameters of the microbolometer element (i.e., α, I_B, R, G_e, and τ_e,) have been measured or derived from other measurements. Alternatively, S_V* may be determined from measurements of the thermal properties of the bolometer's I-V curve (*12*).

With regards to NEP, it may be found using equation 1 and the results of independent determinations of V_n and S_V. In this case V_n also is obtained from electrical measurements, but the voltage responsivity is obtained from measurements with a blackbody source or a monochromatic optical or RF source.

Care must be taken to note the exact conditions under which the detector NEP is determined, in order for it to be interpreted properly (*16*). Conditions that need to be specified include whether the input power was from a monochromatic or a blackbody source and whether the total rms input power uniformly illuminated the aperture of the primary collecting optics. Also note the center frequency and bandwidth of the RF source, the modulation frequency, and the video bandwidth of the output detector.

The rms noise and output voltages must be measured at the same circuit point. If this point is at the output of a preamplifier, the characteristics of the latter must be specified. Since the voltage measurement may be made with a larger than unity bandwidth, the manner in which the noise voltage was normalized to the square root of unity bandwidth must be indicated. This is especially important if the noise voltage is not uniform over the video bandwidth.

2.2.2 Noise Equivalent Temperature Difference

A frequently used figure of merit for infrared detectors, that is also applicable for MMW microbolometer detectors, is the noise equivalent temperature difference, or NETD (*18*). If the aperture of a radiometer is uniformly illuminated by a blackbody source with temperature T, then its NETD can be defined as that change in temperature, ΔT, of the blackbody source that is required to change the output rms signal-to-noise voltage ratio of the detector by unity. The NETD has units of degrees K, and it is the same as the ΔT_{min} figure of merit commonly used to characterize microwave and MMW radiometers.

The NETD of a MMW microbolometer detector, such as shown schematically in figure 2, can be expressed as

$$NETD = \frac{NEP(B_v)^{\frac{1}{2}}}{\Delta P_{in}/\Delta T}, \tag{21}$$

where

NEP = the noise equivalent power of the microbolometer,

B_v = the video bandwidth of the receiver,

P_{in} = the power incident on the aperture of the secondary collecting optics from a blackbody source with temperature T, and $\Delta P_{in}/\Delta T$ = the change in the incident power from the blackbody source per unit change in its temperature.

Consider a MMW radiometer with a microbolometer detector, such as shown schematically in figure 1. If P is the power from a blackbody source with temperature T and it is incident uniformly on the aperture of the primary collecting optics, then P_{in}, the power incident on the aperture of the secondary collecting optics, is $P_{in} = \rho_0 P$, where ρ_o is the transmission efficiency of the primary collecting optics. The MMW power received from a blackbody source by a MMW radiometer is, from the Rayleigh-Jeans approximation for Planck's radiation law, $P = kTB_{RF}$, where B_{RF} is the radiometer RF bandwidth. Then $\Delta P_{in}/\Delta T = \rho_o k B_{RF}$, and the NETD of the MMW radiometer is given by

$$\mathrm{NETD} = \frac{\mathrm{NEP}\left(B_v\right)^{\frac{1}{2}}}{\rho_o k B_{RF}}. \tag{22}$$

3. Status of Microbolometer Developments

3.1 Uncooled MMW/Sub-MMW Detectors

The electrical noise equivalent powers, NEP*'s, obtained for several uncooled MMW and sub-MMW microbolometer elements are given in table 1. Also listed in the table is the optical noise equivalent power, NEP, for the MMW microbolometer reported by Anderson et al., (*10*). The techniques used to determine the NEP*'s and the NEP's were discussed in the previous section.

Table 1. Characteristics of several uncooled MMW and sub-MMW microbolometer detectors. Listed for each is its electrical noise equivalent power, NEP*, except for the one noted. Also listed for each are the bolometer film and substrate materials, the radiation frequency, ν, the modulation frequency, f_m, and the thermal time constant, τ.

ν(GHz)	Material	NEP* $\left(\mathrm{pW}/\sqrt{\mathrm{Hz}}\right)$	f_m(Hz)	τ(s)	Reference
95	$Nb/SiO_2/Si$	100	10^3	0.18×10^{-6}	(*21*) McDonald et al. (*22*) Grossman et al.
95	$Nb/Si_3N_4/Si$	83	10^3	–	(*6*) Rahman et al.
500	Nb/Polyimide/Si	15	10^3	$<1.5 \times 10^{-6}$	(*7*) Luukanen et al.
95	$VO_x/Si_3N_4/Si$	$12^{\oplus}$	10	25×10^{-3}	(*10*) C. Anderson et al.

⊕ NEP value (from extrapolation to peak spectral response)

Microbolometers fabricated with vanadium oxide (VO_x) films have received considerable attention for applications in uncooled IR microbolometers (*24*) due to the relatively high temperature coefficient of resistance of VO_X. An uncooled MMW microbolometer array fabricated with this material and integrated with an uncooled IR VO_X microbolometer detector array would have potential for a number of applications, if the sensitivity of the MMW detector can be made high enough for passive imaging. Note that the NEP reported for the MMW VO_x microbolometer in table 1 was determined using a modulation frequency of 10 Hz. Since the thermal time constant of this microbolometer is relatively long, its NEP would be much higher if it had been measured at 1 kHz.

It can be seen from equation 19 that the NETD of the microbolometer varies directly as the NEP and inversely as the RF bandwidth. In practice, the size of the RF bandwidth may be limited by the extent to which the characteristics of the primary and the secondary collecting optics change with frequency and also by the attenuation characteristics of the environment in which the radiometer is to be operational. If the radiometer is to operate in the atmosphere, the contrast in the image of the scene being displayed will decrease in proportion to the average attenuation of the atmosphere in the path between the scene and the sensor for all the frequencies its RF bandwidth (*23*). For example, oxygen absorption lines at 60 and 120 GHz may make it inadvisable to design a radiometer to include one or both of these frequencies in its bandpass. In addition, if the image contrast depends on the sky having a low brightness temperature, any oxygen absorption line that lies within the radiometer's RF bandwidth will tend to raise the average sky brightness temperature and thereby degrade the image contrast. Similar effects will occur for any other operational scenario, if the media has any strong absorption bands or lines in the radiometer's RF bandwidth.

The dependence of a radiometer's NETD on the NEP of its detector given in equation 22 is shown plotted in figure 4 for values of the RF bandwidth, B_{RF}, equal 20, 40, and 70 GHz. The video bandwidth, B_v, was taken to be 30 Hz, and the transmission efficiency of the primary collecting optics, ρ_o, was equal to 0.50. The NETDs calculated for the NEP reported by Anderson et al., (*10*) are indicated in the figure for values of B_{RF} = 40 and 70 GHz. The 40-GHz RF bandwidth may be easier to achieve than the 70 GHz value for a radiometer with a center frequency of around 95 GHz. Designing the primary and secondary collecting optics to meet performance specifications over the relatively large fractional bandwidth of 70 GHz could be a problem. This could be true especially if a maximum number of microbolometer detectors in the focal plane array (FPA) of the radiometer is needed.

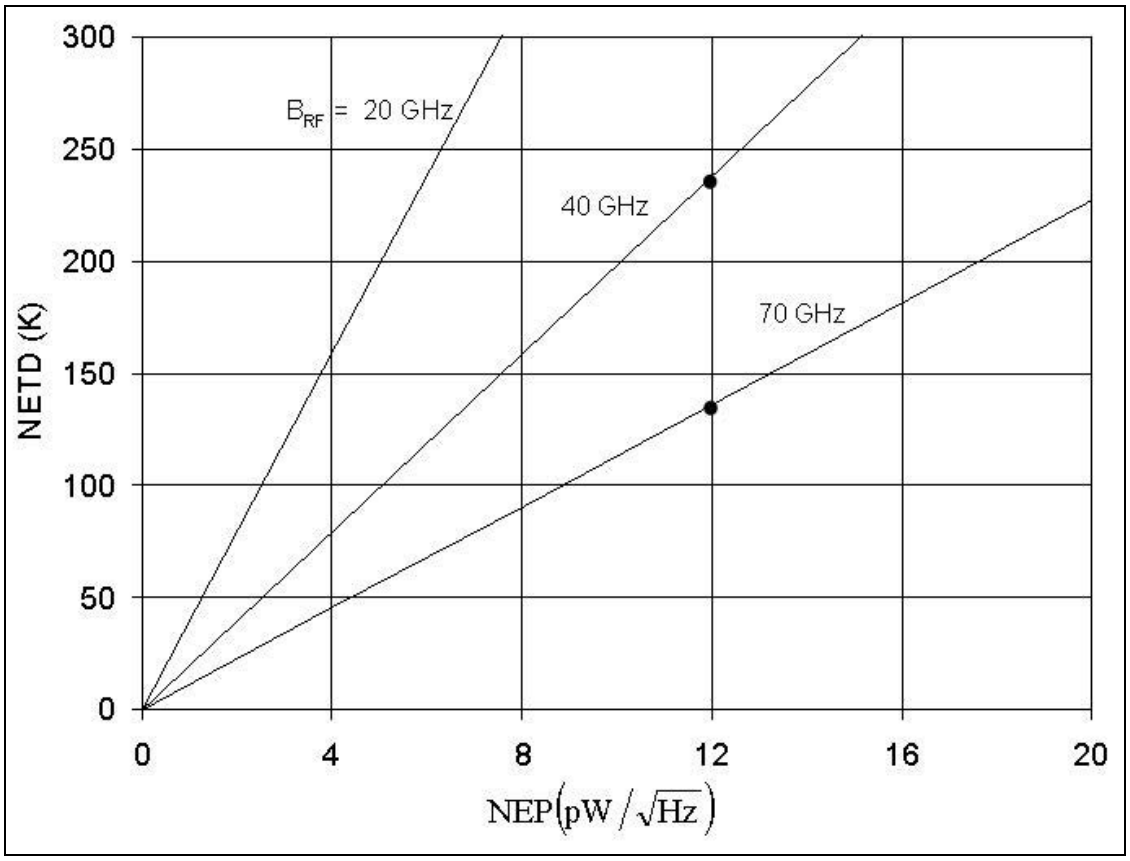

Figure 4. NETD of an uncooled MMW radiometer shown plotted as a function of the NEP of its microbolometer detector for three values of the RF bandwidth, B_{RF}. The video bandwidth, B_V, was taken to be 30 Hz, and the transmission efficiency of the primary collecting optics, ρ_0, was 0.50. The NETD's calculated for the NEP = 12 pW/(Hz)$^{1/2}$, reported by Anderson et al., (*10*), are indicated.

A MMW or sub-MMW radiometer needs to have an NETD of about 6 K or less in order for it to meet the minimum requirements for many applications. The results in figure 4 show that the NETD of the uncooled MMW microbolometer with the lowest NEP that has been reported to date cannot meet this requirement. This leads us to the next section to see whether the developments of far-infrared and IR microbolometers, using different bolometer materials, show results that might suggest an approach for improving the current performance of uncooled MMW microbolometers.

3.2 Uncooled Infrared Detectors

Considerable effort has gone into the development of uncooled detectors that have sufficient sensitivity for many infrared imaging applications. This effort has led to the development of materials that have a relatively high temperature coefficient of resistance and other properties that make them suitable for possible use in infrared microbolometer FPAs. Prominent amongst these materials are VO_x, amorphous silicon (α-Si), and yttrium barium copper oxide (YBCO). These materials are semiconductors at room temperature, and YBCO also is a high temperature

superconductor material that undergoes a transition to a superconducting state at temperatures of between 80 K and 95 K, depending on its exact composition. The temperature coefficients of resistance of these materials at room temperature are –2%/K for VO_x, –2.5% /K for α-Si, and higher than –3%/K for YBCO (*26*).

It was indicated in the previous section that a MMW microbolometer already has been fabricated using VO_x, but that the NEP reported for this detector needs to be much lower before it can meet the requirements for passive imaging applications. However, it can be useful to use the VO_x infrared microbolometer performance as a benchmark for comparing it with those for the other two materials. The performance of these uncooled infrared microbolometers might suggest possibilities for development of a sensitive MMW microbolometer. The results obtained for microbolometer FPA's that were fabricated with the three different materials by three different laboratories are summarized in table 2. Their NETD's were measured with blackbody sources, and each had FPA's with 320×240 elements. The array pitches ranged between 25 and 40 micrometers. The NEP's of these detectors were not reported.

Table 2. Characteristics of several uncooled infrared microbolometers focal-plane-array detectors. Listed for each is its NETD and the materials used for its bolometer film and substrate. λ gives the wavelength range and f_m is the modulation frequency used for the measurement.

λ(μm)	Material	NETD(mK)	f_m(Hz)	Reference
8-14	$VO_x/Si_3N_4/Si$	35	30	(*24*) D. Murphy et al.
8-12	α-Si:H/ Polyimide/Si	36	50	(*25*) Mottin et al.
8-12	YBCO/ SiO_2/Si	80	30	(*26*) Wada et al.

Caution is needed when estimating how these infrared detector results would carry over to MMW detectors, since a detector's NETD is determined by a number of detector design parameters that may vary with its operational frequency. However, it is probably safe to say that an uncooled MMW microbolometer built with either α-Si or YBCO material would not have a much lower NEP than the one that was built with VO_x. These results strongly suggest that the prospects for fabricating a sufficiently sensitive uncooled MMW microbolometer with other materials do not look very promising at this time. This leads us to the next section in which the results obtained for cooled far-infrared/infrared microbolometers are reviewed to see what they might suggest for possible development of a sensitive MMW microbolometer.

3.3 Cooled Far-Infrared/Infared Detectors

Research on far-infrared/infrared thermal detectors for astronomical and spectroscopic investigations showed that sensitive detectors could be developed using materials that became superconducting when cooled to liquid helium temperatures. These materials have a high rate of change resistance when they go from a normal to a superconducting state with the result that they are very sensitive bolometers when operated around their superconducting transition temperature

(*12, 27*). However, interest in these transition-edge type bolometer detectors waned after other liquid-helium cooled detectors were found to have a higher sensitivity, until the discovery of high temperature superconductor (HTSC) materials that became superconducting at about liquid nitrogen temperatures. Detectors that operate at about liquid nitrogen temperatures are much more acceptable for many applications than those that require being cooled to liquid helium temperatures, especially since relatively low-cost closed-cycle refrigerators (cryocoolers) are available. These transition-edge bolometer detectors also are attractive for far-infrared/infrared applications because, being thermal detectors, they can have good sensitivity over a wide range of wavelengths. There are other liquid-nitrogen cooled detectors that are very sensitive in the 8-12 μm wavelength, but they are not very sensitive for wavelengths above about 12 μm. The interest in imaging astronomical events at far-infrared and infrared wavelengths has resulted in considerable progress being made in the development of HTSC microbolometer detectors.

The most recent results that have been obtained with HTSC far-infrared/infrared microbolometers are summarized in table 3. The HTSC materials used for the microbolometers were epitaxial films of either YBCO, Cobalt doped-YBCO (Co-YBCO), or gadolinium barium copper oxide (GBCO). The measurements were made at the transition temperature of the material used for each microbolometer, between 83 K and 90 K. The NEP listed in the table for each microbolometer was determined from optical measurements, except for the work by Sanchez et al., (*31*). In that case the NEP was estimated using the value they reported for NEP* and the collection efficiency, ρ_a, that they expect to achieve for an infrared absorption layer on the bolometer.

Table 3. Characteristics of several far-infrared/infrared cooled HTSC microbolometer detectors. The NEP and the type of material used for the bolometer and its substrate are listed for each. λ is the wavelength range and f_m is the modulation frequency used for the measurements. The thermal time constant, τ, also is listed.

λ(μm)	**Material**	**NEP** $\left(\mathbf{pW}/\sqrt{\mathbf{Hz}}\right)$	**f_m(Hz)**	**τ(ms)**	**Reference**
12-36	Co-YBCO/ $LaAlO_3$	0.63	32	—	(*28*) Berkowitz et al.
8-12	YBCO/Si	8.7	254	0.56	(*29*) Mechin et al.
70-200	GBCO/ Si_3N_4	5.5	2	115	(*30*) de Nivelle et al.
84	GBCO/ Si_3N_4	5.3⊕	5	27	(*31*) Sanchez et al.
1–5	YBCO/–	2.3	15	—	(*32*) Xinyu Zhang et al.

⊕ Estimated from the reported NEP* = 3.7 pW/$\sqrt{\mathbf{Hz}}$ and the expected collection efficiency $\rho_a = 0.7$.

To compare the results obtained for the uncooled microbolometers in table 1 and the cooled ones listed in table 3, recall that the NEP of a microlometer is always larger than the NEP* of its element. Since the NEP's of the cooled microbolometers listed in table 3 are much lower than the NEP*s of the uncooled detector elements, the average NEP* of the cooled microbolometer elements will certainly also be less than that of the uncooled elements. Although there are some differences in the design of a microbolometer for a MMW detector and one for a far-infrared or

infrared detector, one can expect from the above results that a cooled MMW HTSC microbolometer element will have an NEP* that is much lower than that of a similarly designed uncooled element. In the next section this conjecture is explored, and the results of calculations are presented for the NEP* of a cooled HTSC microbolometer element and the NETD of a MMW radiometer with such a cooled HTSC microbolometer element.

4. MMW Cooled Microbolometer Detector

4.1 NEP* of a HTSC Microbolometer Element

The expected performance of a MMW HTSC microbolometer detector can be calculated, once its basic parameters have been specified, using the equations for the detector's figures of merit given in section 2.2. A key part of the detector is the microbolometer element, and achievable values of its basic parameters may be inferred from the results that have been reported for cooled far-IR/IR microbolometer detectors. Selected values from these reports are given in table 4. They should be applicable for estimating the performance of the element of a MMW HTSC detector, since the properties of a composite microbolometer element are almost independent of the radiation's wavelength once the radiation has been converted into thermal energy. The parameter values listed in table 4 have therefore served as a guide for defining a base-line set used to make the NEP calculations that will follow. This base-line set of values are those listed for case 1 in table 5.

Table 4. Selected values of the basic parameters of HTSC microbolometer elements that have been reported in the literature.

Parameter	Value	Reference
Thermal instability coefficient, $a = \alpha I_B R/G$	0.3	(*19*)
Temperature coefficient of resistance, α (K^{-1})	1	(*33, 34*)
Heat capacity, C (J/K)	0.96×10^{-9}	(*28*)
Thermal conductance, G (W/K)	0.85×10^{-7}	(*34*)
1/f noise coefficient, n	0.20×10^{-13}	(*35*)
Microbolometer resistance, R (Ω)	75	(*36*)
HTSC transition temperature (nominal), T(K)	90	(*19*)

Table 5. The various sets of values of the basic parameters of a HTSC microbolometer element that were used to calculate the electrical noise equivalent power, NEP*, of the element as a function of the modulation frequency, f_m. Also listed for each case is the value of the thermal time constant $\tau = C/G$. Case 1 is termed the base-line case.

	Parameter Values				
CASE NO.	**α (K^{-1})**	**C (J/K)**	**G (W/K)**	**n**	**τ (ms)**
1	1	1×10^{-9}	1×10^{-7}	1×10^{-13}	10
2	1	1×10^{-9}	1×10^{-8}	1×10^{-13}	100
3	1	1×10^{-9}	1×10^{-6}	1×10^{-13}	1
4	1	1×10^{-10}	1×10^{-7}	1×10^{-13}	1
5	1	1×10^{-8}	1×10^{-7}	1×10^{-13}	100
6	2	1×10^{-9}	1×10^{-7}	1×10^{-13}	10
7	0.10	1×10^{-9}	1×10^{-7}	1×10^{-13}	10
8	1	1×10^{-9}	1×10^{-7}	1×10^{-11}	10
9	1	1×10^{-9}	1×10^{-7}	1×10^{-10}	10
10	1	1×10^{-10}	1×10^{-8}	1×10^{-13}	10

If a microbolometer element has constant-current bias source, its NEP* may be determined from the ratio of V_n and S_V* calculated using equations 9, 10, and 11 or directly from equation 18. The results of separate calculations for V_n, S_V*, and their ratio can be useful for examining exactly how the different intrinsic noise sources and the responsivity contribute to the element's NEP*. Such separate calculations were made using values of the parameters listed for case 1 in table 5, the microbolometer resistance, R, equal to 75 Ω, taken from Rice et al., (*36*), and the bias current, I_B, determined to be 20 μA from equation 15 with a = 0.3, for the thermal instability coefficient, and Rice's value of R. The temperature, T, was assumed to be 90 K, a nominal value for the transition temperature of the HTSC YBCO.

The results of the calculations for S_V*, the intrinsic rms noise voltages, V_{ph}, $V_{1/f}$, and V_J, and the total intrinsic noise voltage, V_n, are given in table 6 for several values of the modulation frequency, f_m. It is seen that S_V* has a relatively high value of 21.4 kV/W when f_m = 1 Hz, but the 10 ms time constant causes it to roll off with f_m to a value of 2.4 kV/W at 100 Hz. This rolloff in S_V* also affects the value of the phonon noise, V_{ph}, since it is linearly dependent on S_V*. The calculations show that the phonon noise is the major contributor to the total noise voltage, V_n, out to about f_m = 80 Hz.

Table 6. HTSC microbolometer element electrical voltage responsivities, S_V*'s, the noise voltages for each of the intrinsic noise sources, and the total intrinsic noise voltages, V_n's, calculated for various values of the modulation frequency, f_m. The calculations were performed using the values of the parameters given in table 5 for Case 1, the base-line case.

	f_m (Hz)					
	1	10	30	50	70	100
$S_V^*(kV/W)$	21.4	16.5	7.5	4.6	3.4	2.4
$V_{ph}(nV/\sqrt{Hz})$	4.5	3.5	1.6	1.0	0.7	0.5
$V_{l/f}(nV/\sqrt{Hz})$	0.5	0.2	0.1	0.1	0.1	0.0
$V_J(nV/\sqrt{Hz})$	0.6	0.6	0.6	0.6	0.6	0.6
$V_n(nV/\sqrt{Hz})$	4.6	3.5	1.7	1.2	0.9	0.8

For low values of the modulation frequency, the relatively high value of the voltage responsivity helps to suppress the 1/f and Johnson noise contributions to the total NEP*. From table 7 it is seen that the value of NEP* is primarily determined by the phonon noise contribution from f_m = 1 Hz to about 80 Hz, i.e., it is at the phonon limit in this frequency range. However, as the modulation frequency increases, the rolloff in S_V* with modulation frequency causes the contribution of the Johnson noise term to NEP* to increase, and above about f_m = 80 Hz, NEP_J* it is the dominant contributor to NEP*.

Table 7. Contributions to the HTSC microbolometer element's total NEP* by each of the intrinsic noise sources, and NEP* calculated for various values of the modulation frequency, f_m. The calculations were performed using the values of the voltage responsivities and noise voltages given in table 6.

	f_m (Hz)					
	1	10	30	50	70	100
$NEP_{ph}^*(pW/\sqrt{Hz})$	0.21	0.21	0.21	0.21	0.21	0.21
$NEP_{l/f}^*(pW/\sqrt{Hz})$	0.02	0.01	0.01	0.01	0.02	0.02
$NEP_J^*(pW/\sqrt{Hz})$	0.03	0.04	0.08	0.13	0.18	0.26
$NEP^*(pW/\sqrt{Hz})$	0.21	0.21	0.23	0.25	0.28	0.33

The value of NEP* = 0.23 pW/$(Hz)^{1/2}$ at f_m = 30 Hz calculated with the base-line set of element parameters looks very promising for development of a cooled MMW microbolometer detector. This value of NEP* is about equal to that estimated from the report on a cooled HTSC

microbolometer for IR imaging by Berkowitz et al., (*28*), and it is much lower than those obtained for uncooled microbolometer detector elements.

It is of interest, however, to see how sensitive this value of NEP* is with respect to the variations in the value of each element parameter. The succinct form of the equation for NEP* given in equation 18 was convenient to use for this purpose, and these calculations were done with it and the parameters values listed for the various cases in table 5. All of the parameter values listed for case 1 were used for the case 2 to 9 calculations except that, in each of these cases, only one of the parameters G, C, α, or n was varied to determine the degree to which the variation of that parameter affected the value of NEP*. For all cases, the thermal instability coefficient, a, was taken to be 0.3, and the temperature, T, was equal to 90 K.

Figure 5 shows the results of the calculations for the dependence of NEP* on f_m using the parameters for cases 1, 2, and 3 listed in table 5. The curve for case 1 shows how NEP* varies with f_m in more detail than does the tabulation in table 7. The curves for cases 2 and 3 show the effects of only varying the value of the thermal conductance, G, from that used for the calculations of the curve for case 1. These curves were calculated with $G = 1 \times 10^{-7}$ W/K, 1×10^{-8} W/K, and 1×10^{-6} W/K, respectively. Since the value of the heat capacity, C, was 1×10^{-9} J/K for all three cases, the time constant $\tau = C/G$ varied along with G. The time constants for cases 1, 2, and 3 were 10 ms, 100 ms, and 1ms, respectively.

The curve for case 2 in figure 5 shows that lowering the value of G by a factor of 10 results in a sharp drop in the NEP* from that for case 1 when $f_m = 1$ Hz. This is because at 1 Hz the NEP*, for both cases 1 and 2, are at about the phonon limit, which varies as $(G)^{1/2}$. However, since the time constant has increased by a factor of 10 for case 2, NEP* increases rapidly with frequency, and it exceeds that for case 1 when f_m is greater than about 30 Hz. This is caused by the increasing value of the S_V* rolloff coefficient with frequency and the subsequent increase in the NEP_J* contribution to NEP*. Hence, although the lower value of G for case 2 drops the NEP* when $f_m = 1$ Hz, the longer time constant ultimately is responsible for negating this lower NEP* as f_m increases.

Also shown in figure 5 is the curve for NEP* vs. f_m for case 3. The value of G is 10 times higher for this case than it is for case 1, and this results in a correspondingly higher NEP* than that for case 1, even at low frequencies. However, since the time constant is 1 ms in this case, the value of the S_V* rolloff coefficient is less than that for case 1. This results in no significant change in NEP* for modulation frequencies at least up to about 100 Hz.

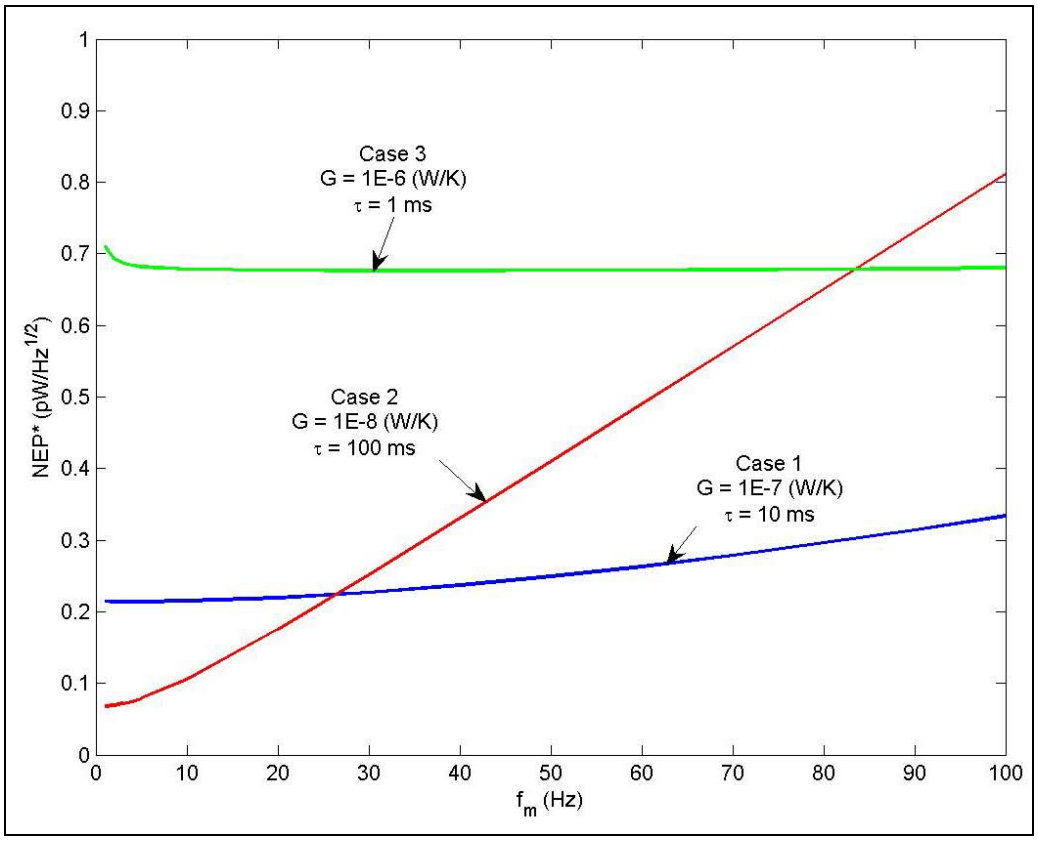

Figure 5. Curves showing the dependence of NEP* on f_m when both G and τ are varied while C and all other parameters are kept constant. The other parameters used for the calculations are listed in table 5.

The curves for NEP* vs. f_m in figure 6 show the results when C (and therefore, also τ) is varied, while G and all the other element parameters are kept constant. The curves for cases 1, 4, and 5 in figure 6 were calculated with $C = 1 \times 10^{-9}$ J/K and τ =10 ms, $C = 1 \times 10^{-10}$ J/K and τ = 1 ms, and $C = 1 \times 10^{-8}$ J/K and τ =100 ms, respectively. It is seen from equation 18 that the only effect of varying C is to change the value of τ. Therefore, the shorter time constant for case 4 results in almost no change in NEP* for f_m between 1 and 100 Hz. However, for case 5 the value of C is larger, and therefore, the time constant is longer. This results in a considerable increase in the Johnson noise contribution to NEP* due to the increase in the rolloff coefficient as f_m increases.

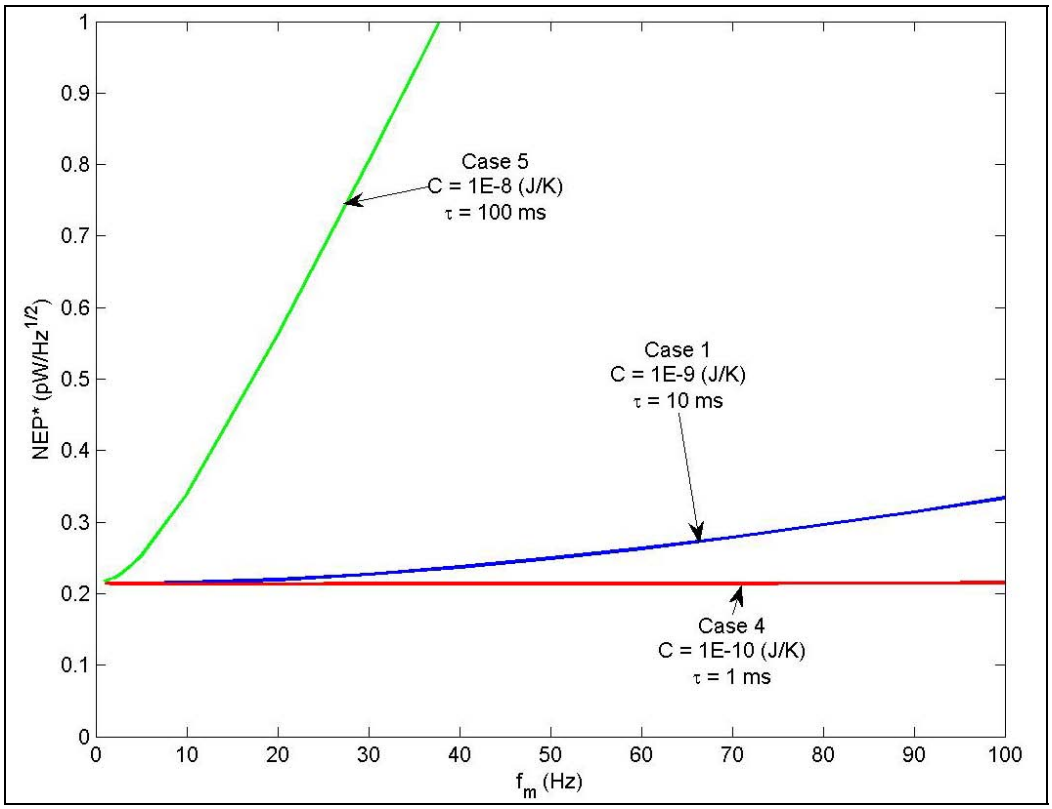

Figure 6. Curves showing the dependence of NEP* on f_m when both C and τ are varied while G and all other parameters are kept constant. The other parameters used for the calculations are listed in table 5.

The effects of only varying the thermal coefficient of resistance, α, on the dependence of NEP* on f_m are seen in figure 7. The values of α for cases 1, 6, and 7 were 1, 2, and 0.1, respectively. Since the thermal time constant is not a function of α, it is seen from equation 18 that changing α only results in changes in the terms that multiply the S_V* rolloff coefficient in $NEP_{1/f}$ and NEP_J*. The calculated NEP* of a microbolometer element with a base-line set of parameters is already at the phonon limit for low modulation frequencies, and the curve for case 6 in the figure shows that raising the value of α from 1 to 2 only reduces NEP* incrementally at $f_m = 30$ Hz. However, if the value of α decreases, the $NEP_{1/f}$* and NEP_J* terms both increase, and NEP* will eventually exceed the phonon limit. The curve for case 7 in figure 7 shows that if $\alpha = 0.1$, the multiplication of the S_V* rolloff coefficient by the $1/\alpha$ terms has caused NEP* to be above NEP_{ph}* for all values of f_m.

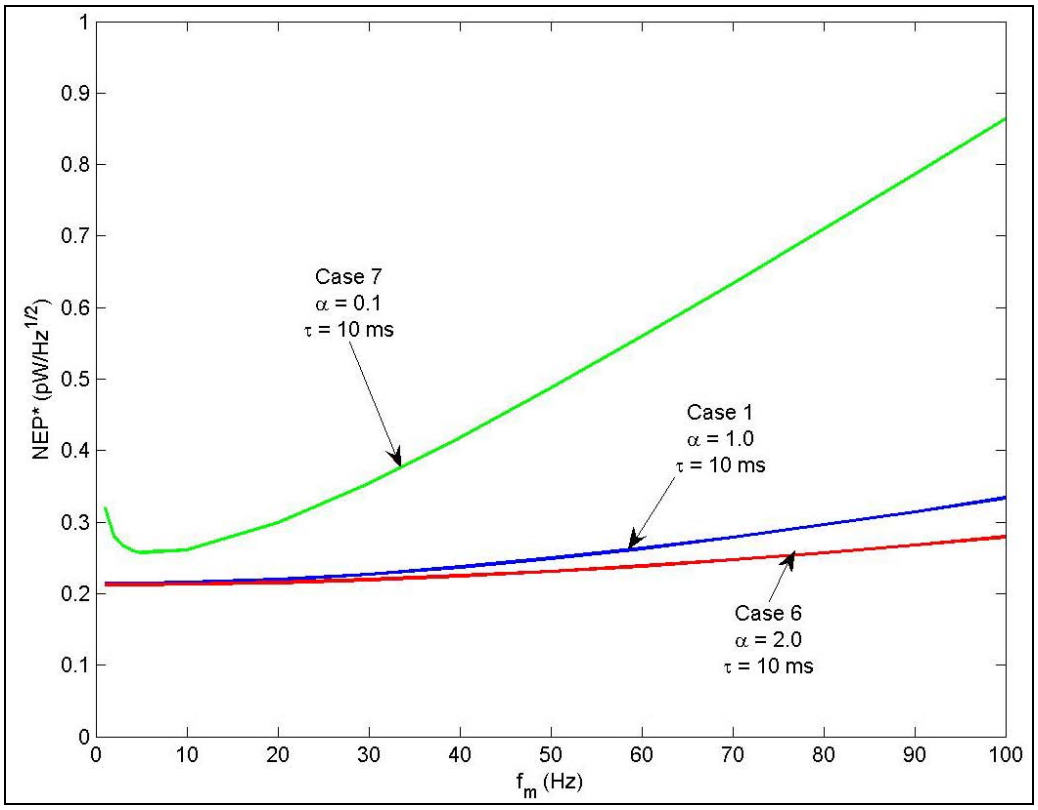

Figure 7. Curves showing the dependence of NEP* on f_m when only α is varied. All other parameters used for the calculations are listed in table 5.

From equation 18 for NEP* it is seen that the effect of lowering the value of the low-frequency noise parameter, n, will be to decrease the $NEP_{1/f}$* term in the equation. As noted above, NEP* calculated with the base-line set of parameters is already at the phonon limit for low frequencies, so decreasing n from its base-line value of 1×10^{-13} only decreases NEP* slightly when f_m = 30 Hz. However, increasing the value of n can result in a higher NEP*. At low frequencies the $(n/f_m)^{1/2}$ factor causes the $NEP_{1/f}$* term to decrease as the frequency increases, but as the frequency increases the S_V* rolloff coefficient increases, and this tends to reverse the $(1/f_m)^{1/2}$ decrease of $NEP_{1/f}$. This effect is illustrated by the curves in figure 8 which show the results when only the value of n in the base-line set of parameters is increased. The values of n for cases 1, 8, and 9 were 1×10^{-13}, 1×10^{-11}, and 1×10^{-10}, respectively. The curves also show that if n is high enough, the result can be that $NEP_{1/f}$* can exceed NEP_{ph}* for all values of f_m.

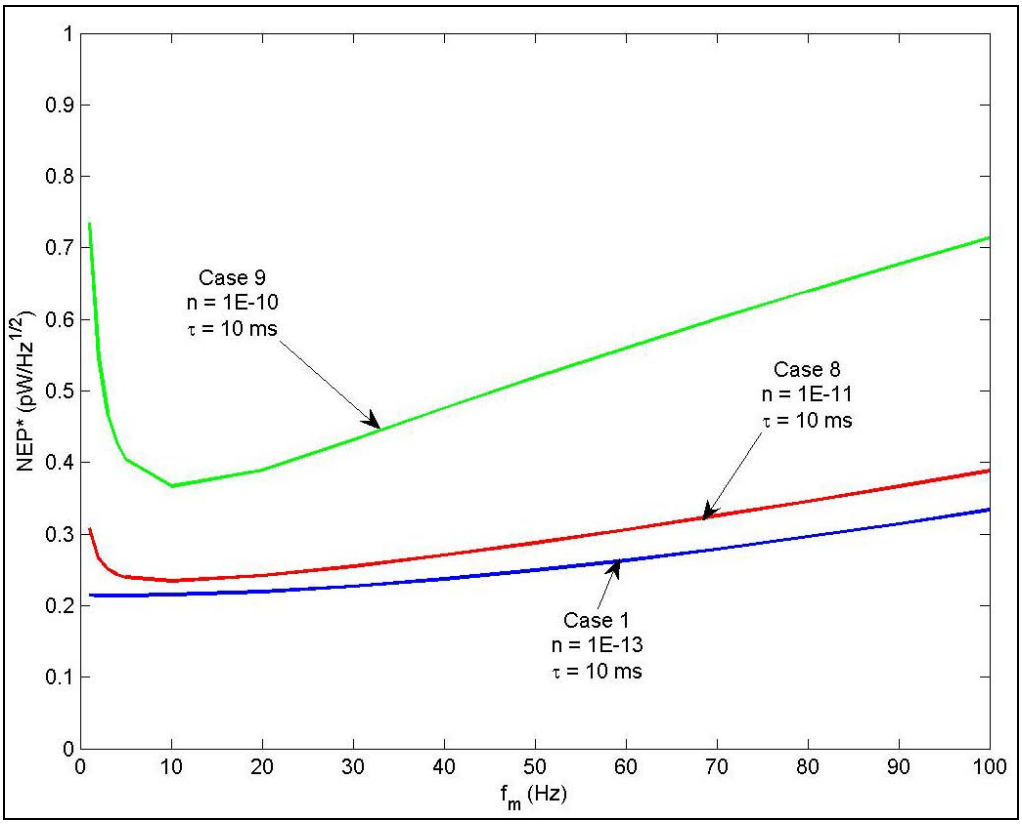

Figure 8. Curves showing the dependence of NEP* on f_m for several values of n.

Previous investigators have indicated the importance of the microbolometer element having a relatively short thermal time constant. The deleterious effects of an inappropriately long time constant was illustrated in the curve for case 2 in figure 5. This curve showed that when G was decreased by a factor of 10 from its base-line value, the element NEP* also dropped at low modulation frequencies. However, since only G was decreased, this resulted in a proportionate increase in the thermal time constant, and in turn, this caused the initially lowered NEP* to increase rapidly as f_m increased. A similar result was apparent in the curve for case 5 in figure 6 when the element also had a relatively long time constant.

The curves for cases 1 and 10 in figure 9 illustrate two cases where the thermal time constant was appropriately short. The curve for case 1 was calculated with $G = 1 \times 10^{-7}$ W/K and $C = 1 \times 10^{-9}$ J/K and that for case 10 was calculated with $G = 1 \times 10^{-8}$ W/K and $C = 1 \times 10^{-10}$ J/K. For case 1 $\tau = 10$ ms, and it was shown earlier that this value is sufficiently short for NEP* to remain below the phonon limit from $f_m = 1$ Hz to about 80 Hz. For case 10, G has dropped by a factor of 10 from the base-line value and at $f_m = 1$ Hz so has NEP*, as it did for case 2. However, since C also has dropped along with G by a factor of 10 from its case 1 value, τ has remained equal to 10 ms. It is seen from figure 9 that this value of the time constant is short enough for NEP* to remain below the phonon limit at least up to $f_m = 100$ Hz.

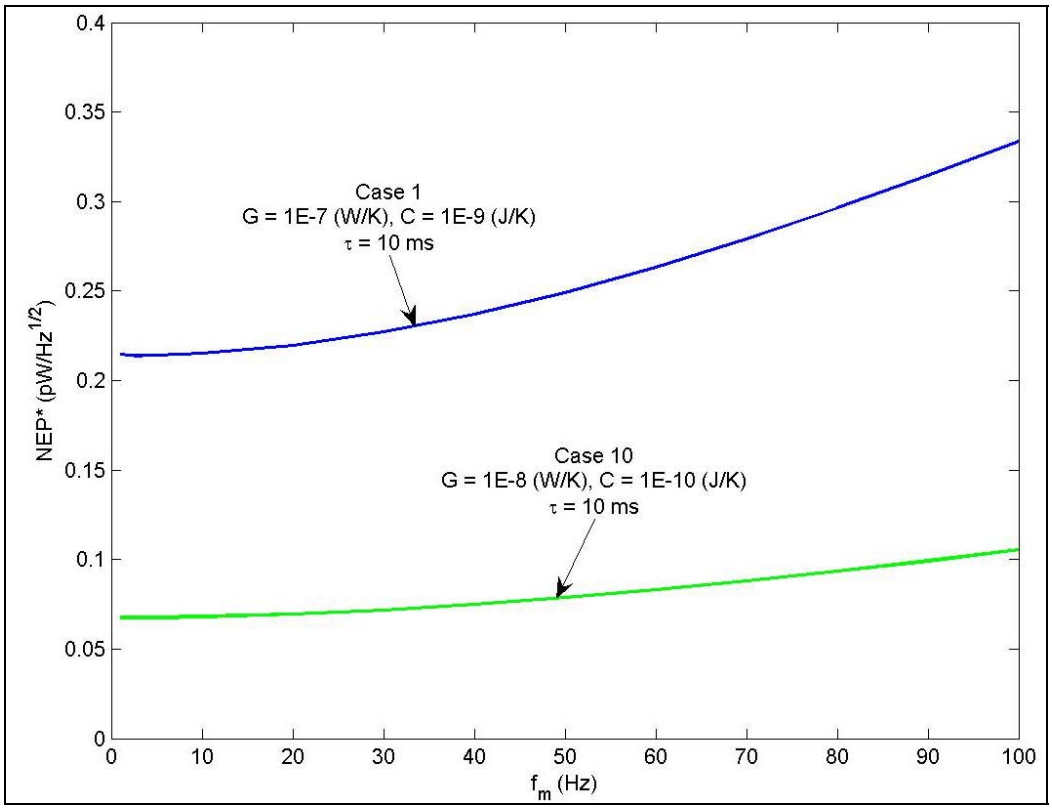

Figure 9. Curves showing the dependence of NEP* on f_m when both G and C are varied, but τ is kept constant. The other parameters used for the calculations are listed in table 5.

4.2 NETD of a MMW Radiometer with an HTSC Microbolometer Detector

Calculations were made in the previous section for the NEP* of an HTSC microbolometer element to allow the NETD of a MMW radiometer with a microbolometer detector to be determined. However, in addition to knowing the NEP* of the element, the transmission efficiencies of both the primary and secondary collecting optics need to be specified before the NETD can be calculated.

The characteristics of several types of microantennas for the secondary collecting optics of IR and MMW microbolometers have been reported by previous investigators (*12*). Specific types of microantennas that have been described include the planar lithographed bow-tie (*37*), the log-periodic (*38*), the log-spiral (*39, 40*), and the micromachined horn (*6*). These types of microantennas have the characteristics needed for the application, namely the potential for high transmission efficiency, ρ_a, and a very wide bandwidth. In general, they have exhibited good performance. For example, the transmission efficiency has been reported to be 0.50 and higher for the log-periodic and log-spiral microantennas (*39, 40, 41*) and 0.90 for a micromachined horn (*42*). For the purposes of the NETD calculations to follow, the assumption is made that a MMW planar lithographed or horn microantenna with $\rho_a = 0.80$ is achievable. In addition, the transmission efficiency of the primary collecting optics, ρ_o, was assumed to be 0.50.

In the previous section, it was shown that the calculated NEP* of a HTSC microbolometer element with an achievable set of base-line element parameters was 0.23 pW/(Hz)$^{1/2}$ at a modulation frequency f_m = 30 Hz. From equation 20, it follows that a MMW HTSC microbolometer detector with such an element and a microantenna with ρ_a = 0.80, would have an NEP equal to 0.29 pW/(Hz)$^{1/2}$. Also in the previous section, a further calculation for the NEP* of a microbolometer element was made assuming that, as a goal, the values of the element parameters G and C could each be lowered an order of magnitude from their base-line values. The result of that calculation was that the element's NEP* would be equal to 0.07 pW/(Hz)$^{1/2}$ at f_m = 30 Hz. With such an element NEP and a microantenna with ρ_a = 0.80, it also follows that this microbolometer detector would have an NEP = 0.09 pW/(Hz)$^{1/2}$.

Equation 22 was used to calculate the NETD of a MMW radiometer vs. the NEP of its HTSC microbolometer detector, and the results are shown plotted in figure 10 for 3 values of the RF bandwidth, B_{RF}. The post-detection (video) bandwidth, B_V, was taken to be 30 Hz. Indicated in the figure are the NETD's of the radiometer if its detector element has the base-line set of parameter values and the detector NEP = 0.29 pW/(Hz)$^{1/2}$. Also shown in the figure are the NETD's if the element has the lower values of G and C discussed above and a detector NEP = 0.09 pW/(Hz)$^{1/2}$.

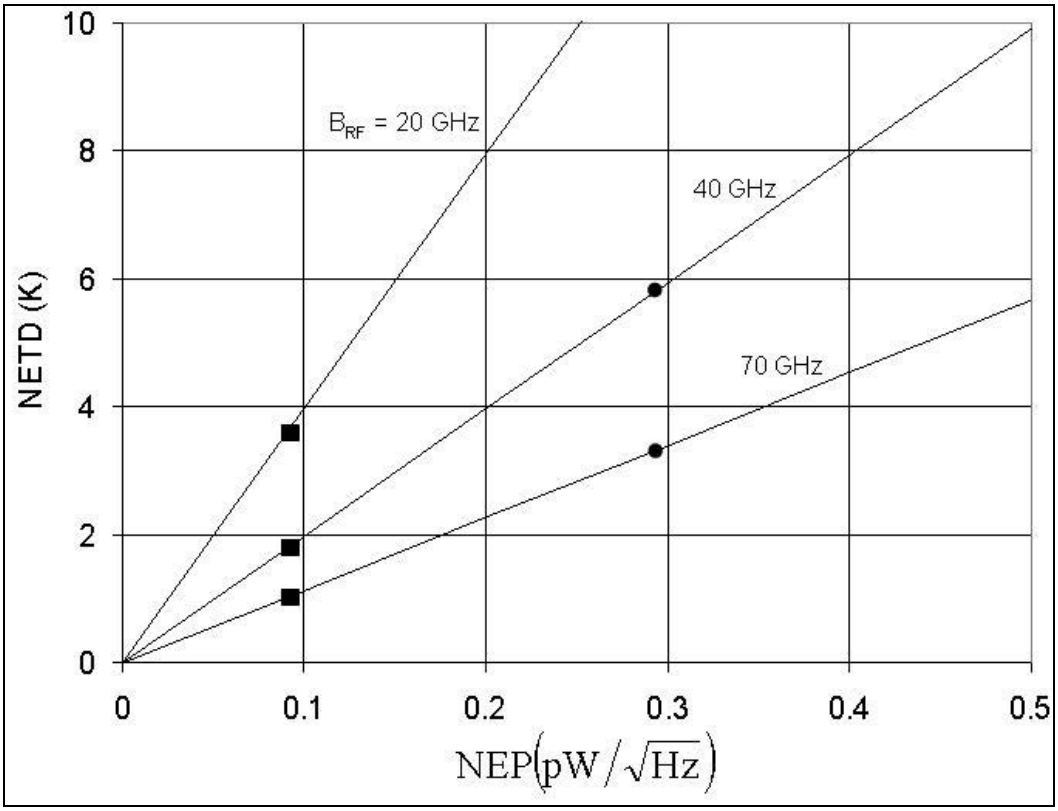

Figure 10. NETD of a cooled MMW radiometer shown plotted as a function the NEP of its HTSC microbolometer detector for three values of the RF bandwidth, B_{RF}. The video bandwidth, B_V, was taken to be 30 Hz, and the transmission efficiency of the primary collecting optics, ρ_o, was 0.5. The NETD's corresponding to detector NEP's equal to 0.09 and 0.29 pW/(Hz)$^{1/2}$ are indicated.

5. Discussion

The review in section 3 of previous microbolometer detector developments showed that uncooled microbolometers do not appear to have the potential to be sensitive enough for application in passive MMW imaging sensors, but the results obtained for IR microbolometers fabricated with a cooled HTSC material suggested that this type detector might be sufficiently sensitive. The calculations in section 4 were made to see whether this could be possible.

Reports on cooled IR HTSC microbolometers were reviewed to determine achievable values for the various microbolometer element parameters. Since the element parameters are mostly independent of the detector's operating wavelength, these results served as a guide for establishing a base-line set of parameter values for calculating the NEP* of a cooled MMW microbolometer. The results of the calculations in section 4 showed that a microbolometer element having parameters with the base-line set of values would have an NEP* = 0.23 $pW/(Hz)^{1/2}$ when $f_m = 30$ Hz. This calculated result compares favorably with the experimental NEP* values from reports on cooled IR HTSC microbolometer detectors (*28, 29*).

Calculations also were made for the NETD of a passive MMW microbolometer detector with an element having the base-line set of parameter values, a microantenna with a transmission efficiency $\rho_a = 0.80$, and NEP = 0.29 $pW/(Hz)^{1/2}$. The transmission efficiency of the primary collecting optics was assumed to be 0.50, and the video bandwidth of the receiver was taken to be 30 Hz. The NETD for this detector was found to be between 3 and 6 K for an RF bandwidth between 70 GHz and 40 GHz. The RF bandwidth possible for this detector will depend on the properties of the primary collecting optics and also on the intended application of the imager, but in any case, a passive MMW imaging system with a detector having an NETD between 3 and 6 K would be sufficiently sensitive for a number of applications.

Additional calculations were made to investigate how much the NEP* of the HTSC microbolometer element would change when each of the 4 critical parameters was varied in turn from its base-line value. It was found that NEP* did not change significantly when $f_m = 30$ Hz if the 1/f noise parameter, n, was lowered from its base-line value of 1×10^{-13}, or if the temperature coefficient of resistance, α, was raised from its base-line value of 1 K^{-1} to 2 K^{-1}, or if the value of the heat capacity, C, was lowered from its base-line value of 1×10^{-9} J/K to 1×10^{-10} J/K.

The results of these calculations indicate that efforts made to either only lower n, raise α, or lower C from their base-line values will not be very effective for lowering NEP* from its base-line value.

Since the thermal conductance, G, determines the NEP* phonon noise level at low values of f_m, it was found that reducing only G by a factor of 10 from its base-line value resulted in NEP* dropping from 0.23 pW/(Hz)$^{1/2}$ to about 0.07 pW/(Hz)$^{1/2}$ when f_m = 1 Hz. This reduction is in accordance with the phonon noise contribution to NEP* varying as $(G)^{1/2}$. However, the lower value of G results in a longer time constant and NEP* increases significantly with increasing modulation frequency. When f_m = 30 Hz, NEP* already is somewhat higher than its base-line value of 0.23 pW/(Hz)$^{1/2}$.

The net result of these calculations is that NEP* for an element with the base-line set of parameter values is at the phonon limit and lowering it for operation at f_m = 30 Hz requires reducing both G and the thermal time constant, τ. Since τ = C/G, further calculations were made with C and G each reduced by a factor of 10 from their base-line values but with n and α each still at their base-line level. Calculations made with this set of element parameter values showed that NEP* = 0.07 pW/(Hz)$^{1/2}$ when f_m =30 Hz, and it still was at about the same phonon noise level it had when f_m = 1 Hz. Achieving this set of element parameter values can be regarded as goal for obtaining a lower NEP*, and it is termed here as the "goal-set" of parameter values.

Additional calculations were made for the NETD of a MMW imaging radiometer developed with a microbolometer detector element having the goal-set of parameter values. The results were that for an NEP* = 0.07 pW/(Hz)$^{1/2}$ when f_m = 30 Hz, the NETD was between 1 and 2 K for the RF bandwidth between 70 and 40 Hz. In the event that the values of C and G can only be reduced proportionately from their base-line values by less than a factor of 10, then the NETD for this improved radiometer would still be less than that calculated for the base-line case.

The advantages of being able to perform passive imaging with MMW's have been amply reviewed by Yujiri (*1*), but it was noted in section 1 that the video frame-rate Passive MMW Cameras that have been developed require many MMW MMIC amplifiers and are quite costly. The objective of this report has been to determine whether it would be feasible to develop a sufficiently sensitive microbolometer detector. As discussed above, the calculations showed that this objective could be achieved with a cooled HTSC microbolometer. Cooling the detector to obtain the higher sensitivity can be done with relatively inexpensive closed-cycle refrigerators (cryostats) that are commonly used for night vision imaging systems. In addition, since HTSC microbolometer detectors can be fabricated using well established photolithographic and micromachining technologies, the cost of a passive MMW imaging system developed with such a detector should be considerably less those with a detector with many MMW MIMIC amplifiers.

6. Conclusions

A review of reports on microbolometer detectors was conducted to determine the possibility for their application in passive MMW imaging sensors. It was concluded that uncooled microbolometers do not appear to have the potential for meeting the requirements for practical passive MMW imaging applications, but that microbolometer detectors developed with cooled high temperature superconductor (HTSC) materials might be suitable. Calculations were made to determine whether it would be feasible to develop such a detector for a practical passive MMW imager.

A base-line set of achievable parameter values for a microbolometer element was identified and used to calculate the noise equivalent power, NEP*, of the element. The results showed that an HTSC microbolometer element having this set of parameter values would have an NEP* = 0.23 $pW/(Hz)^{1/2}$ when the modulation frequency, f_m, equals 30 Hz.

Calculations also were made for the noise equivalent temperature difference, NETD, of a passive MMW imaging radiometer with such a cooled HTSC microbolometer detector. The results showed that if the element NEP* = 0.23 $pW/(Hz)^{1/2}$, f_m = 30 Hz, and the microantenna transmission efficiency was equal to 0.80, then the radiometer NETD would be between 3 and 6 K for RF bandwidths between 70 and 40 GHz.

A cooled passive MMW imaging sensor array developed with such microbolometer detectors would have performance characteristics competitive with those of previously developed systems, be much less costly than those systems, and be suitable for practical applications. Cooling the HTSC microbolometers could be done with relatively inexpensive cryocoolers commonly used in night vision devices, and fabrication of the detectors could be accomplished at low cost using well established photolithographic and micromachining technology.

Additional calculations were made that showed which of the HTSC microbolometer element parameters in the base-line set need to be changed in order to obtain an even lower NEP*. For this purpose, a goal-set of element parameters was assumed for the calculations. These parameters had the same values as in the base-line set, except that the thermal conductance and heat capacity each was a factor of 10 lower in value than in the base-line set. The result of the calculations with these parameter values was that the microbolometer element NEP* = 0.07 $pW/(Hz)^{1/2}$ when f_m = 30 Hz. The NETD of a radiometer with such a cooled microbolometer detector also was determined and found to be between 1 and 2 K when f_m = 30 Hz and for the RF bandwidth between 70 and 40 GHz. Further work is needed for development of a cooled HTSC microbolometer having the goal-set of element parameters.

7. References

1. Yujiri, L.; Shoucri, M.; Moffa, P. Passive Millimeter-Wave Imaging. *IEEE microwave magazine* **September 2003**, 39–50.

2. Yujiri L.; et al. Passive millimeter-wave camera. *Proc. SPIE* **April 1997**, *3064*, 15–22.

3. Appleby, R.; et al. Compact real-time (video-rate) passive millimetre-wave imager. *Proc. SPIE* **April 1999**, *3703*, 13–19.

4. Martin, C.; Lovberg, J.; Clark, S.; Galliano, J. Real time passive millimeter-wave imaging from a helicopter platform. *Proc. SPIE* **April 2000**, *4032*, 22–28.

5. Martin, C.; Clark, S. E.; Lovberg, J. A.; Kolinko, V. Passive millimeter-wave imaging technology for phased array systems. *Proc. SPIE* **April 2003**, 5077, 33–41.

6. Rahman A.; et al. Micromachined room-temperature microbolometer for mm-wave detection and focal-plane imaging arrays. *Proc. SPIE* **April 1997**, *3064*, 122–133.

7. Luukanen, A.; Viitanen, V.-P. Terahertz imaging systems based on antenna-coupled microbolometers. *Proc. SPIE* **April 1998**, *3378*, 34–44.

8. Nolen, S.; et al. Antenna-coupled niobium bolometers for mm-wave imaging arrays. *Proc. SPIE* **July 1999**, *3795*, 279–286.

9. Milkov, M. M. Millimeter-Wave Imaging System Based on Antenna-Coupled Bolometers. Master of Science Thesis, University of California Los Angeles, 2000.

10. Anderson C.; et al. A 24×24 Bolometer Based Passive Millimeter Wave Imager. *Proc. of Military Sensing Symposium (MSS)*, Parallel Meetings of the MSS Specialty Groups on Passive Sensors, etc., N. Charleston, SC, April 2002.

11. Smith, R. A.; Jones, F. E.; Chasmar, R. P. *The Detection and Measurement of Infrared Radiation*; Clarendon Press: Oxford, 1957, 91–116 and 256–275.

12. Richards, P. L. Bolometers for infrared and millimeter waves. *J. Appl. Phys.* **1 July 1994**, *76* (1), 1–24.

13. Kruse, P. W.; McGlauchlin, L. D.; McQuistan, R.B. *Elements of Infrared Technology: generation, transmission, and detection*; John Wiley & Sons, Inc.: New York, 1962, 131 and 399.

14. Holter, M. R.; Nudelman, S.; Suits, G. H.; Wolfe, W. L.; Zissis, G. J. *Fundamentals of Infrared Technology*; The McMillan Co.: New York, 1962, 176–182.

15. Hudson, R. D. *Infrared System Engineering*; John Wiley & Sons: New York, 1969, 289–296.

16. Limperis, T. *Handbook of Military Infrared Technology*; Chapter 11, W.L. Wolfe, ed.; Office of Naval Research, Dept. of the Navy, Wash., D.C., 1965, 466.

17. Wood, R. A. *Monolithic silicon microbolometer arrays*; *Uncooled Infrared Imaging Arrays and Systems, Semiconductors and Semimetals*, Vol. 47, P. W. Kruse and D. D. Skatrud, eds.; Academic Press: San Diego, 1997, pp. 43–121.

18. Kruse, P. W. *Uncooled Thermal Imaging Arrays, Systems and Applications*; SPIE Press: Bellingham, Washington, 2001, p.8.

19. Richards, P. L.; et al. Feasibility of the high T_C superconducting bolometer. *Appl. Phys. Lett.* **16 January 1989**, *54* (3), 283–285.

20. Lee, A. T.; Richards, P. L.; Nam, S. W.; Cabrera, B.; Irwin, K. D. A superconducting bolometer with strong electrothermal feedback. *Appl. Phys.Lett.* **16 September 1996**, *69* (12), 1801–1803.

21. McDonald, M. E.; Grossman, E. N. Niobium Microbolometers for Far-Infrared Detection. *IEEE Trans. on Microwave Theory and Techniques* **April 1995**, *43* (4), 893–896.

22. Grossman, E. N.; Nolen, S.; Paulter, N.G.; Reintsema, C. D. Concealed weapons detection system using uncooled, pulsed, imaging arrays of millimeter-wave bolometers. *Proc. SPIE* **April 2001**, *4373*, 7–15.

23. Nemarich, J.; Cassidy, T. W. Passive Millimeter-Wave Imaging for Detection of Military Vehicles from Airborne Platforms. *Proc. Fourth Joint International Military Sensing Symposium (MSS)* **December 2000**, *45* (2), 17–34.

24. Murphy, D.; et al. High Sensitivity 25 μm Microbolometer FPAs. *Proc. SPIE* **April 2002**, *4721*, 99–110.

25. Mottin, E.; et al. Uncooled amorphous silicon technology: high performance achievement and future trends. *Proc. SPIE* **April 2002**, *4721*, 56–63.

26. Wada, H.; et al. YBaCuO uncooled microbolometer IRFPA. *Proc. SPIE* **April 2001**, *4369*, 299–304.

27. Kraus, H. Superconductive Bolometers and Calorimeters. *Supercond. Sci. Technol.* **1996**, *9*, 827–842.

28. Berkowitz, S. J.; Hirahara, A. S.; Char, K.; Grossman, E. N. Low noise high-temperature superconducting bolometers for infrared imaging. *Appl. Phys. Lett.* **30 September 1996**, *69* (14), 2125–2127.

29. Mechin, L.; Villegier, J.-C.; Bloget, D. Suspended epitaxial YBaCuO microbolometers fabricated by silicon micromachining: Modeling and measurements. *J. Appl. Phys.* **15 May 1997**, *81* (10), 7039–7047.

30. de Nivelle, M. J. M. E.; et al. Low noise high-T_C superconducting bolometers on silicon nitride membranes for far-infrared detection. *J. Appl. Phys.* **15 November 1997**, *82* (10), 4719–4726.

31. Sanchez, S.; et al. A High-T_C Superconductor Bolometer on a Silicon Nitride Membrane. *IEEE J. Microelectromech. Syst.* **March 1998**, *7* (1), 62–68.

32. Zhang, Xinyu; et al. Linear High-T_C $YBa_2Cu_3O_{7-\delta}$ Superconducting Thin Film Infrared Detectors Coupled with A Cylindrical Microlens Array in Quartz Glass Substrate. *Int'l. J. of Infrared and Millimeter Waves* **1999**, *20* (6), 1047–1058.

33. Verghese, S.; Richards, P. L.; Char, K.; Fork, D. K.; Geballe, T. H. Feasibility of infrared imaging arrays using high-T_C superconducting bolometers. *J. Appl. Phys.* **15 March 1992**, *71* (6), 2491–2498.

34. Johnson, B. R.; Foote, M. C.; Marsh, H. A.; Hunt, B. D. Epitaxial $YBa_2Cu_3O_7$ superconducting infrared microbolometers on silicon. *Proc. SPIE* **July 1994**, *2267*, 24–30.

35. Foote, M. C.; Johnson, B. R.; Hunt, B. D. Transition edge $YBa_2Cu_3O_{7-x}$ microbolometers for infrared staring arrays. *Proc. SPIE* **1994**, *2159*, 2–9.

36. Rice, J. P.; Grossman, E. N.; Rudman, D. A. Antenna-coupled high-T_C air-bridge microbolometers on silicon. *Appl. Phys. Lett.* **8 August 1994**, *65* (6), 773–775, and Rice, J. P.; Grossman, E. N.; Borcherdt, L. T.; Rudman, D. A. High-T_C superconducting antenna-coupled microbolometer on silicon. *Proc. SPIE* **1994**, *2159*, 98–109.

37. Rutledge, D. B.; Neikirk, D. P.; Kasilingham, D. P. *Integrated Circuit Antennas; Infrared and Millimeter Waves*; Vol. 10, K. J. Button, ed.; Academic Press: New York, 1983, Chap. 1.

38. Nahum, M.; et al. Fabrication and Measurement Of High T_C Superconducting Microbolometers. *IEEE Trans. Magn.* **March 1991**, *MAG-27* (2), 3081–3084.

39. Grossman, E. N.; Sauvageau, J. E.; McDonald, D. G. Lithographic spiral antennas at short wavelengths. *Appl. Phys. Lett.* **16 December 1991**, *59* (25), 3225–3227.

40. MacDonald, M. E.; Grossman, E. N. Pattern and polarization measurements of integrated-circuit spiral antennas at 10 μm wavelength. *Proc. SPIE* **April 1996**, *2842*, 501–512.

41. Hu, Q.; Richards, P. L. Design analysis of a high T_C superconducting microbolometer. *Appl. Phys. Lett.* **4 December 1989**, *55* (23), 2444–2446.

42. Ahmad, W. Y. A.; Rebeiz, G. M.; Bishop, W. L.; Crowe, T. W. An 86-106 GHz quasi-integrated low noise Schottky receiver. *IEEE Trans. on Microwave Theory and Techniques* **April 1993**, *41* (4), 558.

Distribution List

ADMNSTR
DEFNS TECHL INFO CTR
ATTN DTIC-OCP (ELECTRONIC COPY)
8725 JOHN J KINGMAN RD STE 0944
FT BELVOIR VA 22060-6218

DARPA
ATTN IXO S WELBY
ATTN MTO M ROSKER
ATTN MTO M STICKLEY
ATTN MTO R BALCERAK
3701 N FAIRFAX DR
ARLINGTON VA 22203-1714

OFC OF THE SECY OF DEFNS
ATTN ODDRE (R&AT)
THE PENTAGON
WASHINGTON DC 20301-3080

CECOM NVESD
ATTN AMSEL-RD-NV-OD F MILTON
ATTN AMSEL-RD-NV-TISD F PETITO
ATTN AMSRD-CER-NV-OD J RATCHES
ATTN AMSEL-RD-NV J BROWN
ATTN AMSEL-RD-NV S HORN
10221 BURBECK RD STE 430
FT BELVOIR VA 22060-5806

US ARMY AMCOM/AATD
ATTN AMSAM-AR-T-I B BUCKANIN
BLDG 401
FT EUSTIS VA 23604-5577

US ARMY AVIATION & MIS LAB
ATTN AMSRD-AMR-SG-IP
H F ANDERSON
BLDG 5400
REDSTONE ARSENAL AL 35809

DIRECTOR
US ARMY RSRCH LAB
ATTN AMSRD-ARL-RO-D JCI CHANG
ATTN AMSRD-ARL-RO-PP D D SKATRUD
PO BOX 12211
RESEARCH TRIANGLE PARK NC 27709

US ARMY RSRCH LAB
ATTN AMSRD-ARL-D J M MILLER
ATTN AMSRD-ARL-CI-OK-T TECHL PUB
(2 COPIES)
ATTN AMSRD-ARL-CI-OK-TL TECHL LIB
(2 COPIES)
ATTN AMSRD-ARL-SE J PELLEGRINO
ATTN AMSRD-ARL-SE-E G WOOD
ATTN AMSRD-ARL-SE-E H POLLEHN
ATTN AMSRD-ARL-SE-EM G SIMONIS
ATTN AMSRD-ARL-SE-EM
V SWAMINATHAN
ATTN AMSRD-ARL-SE-R
ATTN AMSRD-ARL-SE-RE D POTREPKA
ATTN AMSRD-ARL-SE-RE M PATTERSON
ATTN AMSRD-ARL-SE-RE S TIDROW
ATTN AMSRD-ARL-SE-RL M DUBEY
ATTN AMSRD-ARL-SE-RL P AMIRTHARAJ
ATTN AMSRD-ARL-SE-RM C LY
ATTN AMSRD-ARL-SE-RM D WIKNER
ATTN AMSRD-ARL-SE-RM E ADLER
ATTN AMSRD-ARL-SE-RM E BURKE
ATTN AMSRD-ARL-SE-RM J NEMARICH
(5 COPIES)
ATTN AMSRD-ARL-SE-RM R WELLMAN
ATTN IMNE-ALC-IMS MAIL & RECORDS
MGMT
ADELPHI MD 20783-1197